

**Flume investigation of bed morphology, flow field, and bed load transport as mechanisms responsible for particle sorting in gravel-bed meandering channels**

**Daniel C. White<sup>1</sup>, Peter A. Nelson<sup>1</sup>**

<sup>1</sup>Department of Civil and Environmental Engineering, Colorado State University, Fort Collins, Colorado, USA.

Corresponding author: Daniel White ([danny.white@colostate.edu](mailto:danny.white@colostate.edu))

**Key Points:**

- Selective transport is likely a controlling mechanism of sorting patterns in gravel-bed meandering channels.
- Coarse gravel patches in pools result from the winnowing of fine sediment by secondary, helical flows.
- The divergence of shear stress on point bars is accommodated by deposition of fine particles producing fine patches.

1 **Abstract**

2 Meandering gravel-bed rivers tend to exhibit bed surface sorting patterns with coarse particles  
3 located in pools and fine particles on bar tops. The mechanism by which these patterns emerge  
4 has been explored in sand-bed reaches; however, for gravel-bed meandering channels it remains  
5 poorly understood. Here we present results from a flume experiment in which bed morphology,  
6 velocity, sediment sorting patterns, and bed load transport were intensively documented. The  
7 experimental channel is 1.35 meters wide, 15.2 meters long, and its centerline follows a sine-  
8 generated curve with a crossing angle of 20 degrees. Water and sediment input were held  
9 constant throughout the experiment and measurements were collected under quasi-equilibrium  
10 conditions. Boundary shear stress calculated from near-bed velocity measurements indicates that  
11 in a channel with mild sinuosity, deposition of fine particles on bars is a result of divergent shear  
12 stress at the inside bend of the channel, downstream of the apex. Boundary shear stress in the  
13 upstream half of the pool was below critical for coarse particles ( $>8$  mm), leading to an armored  
14 pool. Inward directed selective transport was responsible for winnowing of fine particles in the  
15 pool. Fine and coarse sediment followed similar trajectories through the meander bend, which  
16 contrasts earlier studies of sand-bedded meanders where the loci of fine and coarse particles  
17 cross paths. This suggests a different sorting mechanism for gravel bends. This experiment  
18 shows that a complex interaction of quasi-equilibrium bed topography, selective sediment  
19 transport, and secondary currents are responsible for the sorting patterns seen in gravel-bed,  
20 meandering channels.

21 **Plain Language Summary**

22 Meandering gravel-bed rivers tend to have large sediment particles located in pools and fine  
23 sediment particles on bar tops. To investigate this pattern, we performed an experiment in a

24 constructed meandering channel. We pumped a constant rate of water and fed sand to pea-size  
25 gravel into the channel. We mapped sediment sorting patterns, measured flow velocities,  
26 calculated force on the channel bed, and measured the movement of sediment. Dynamic  
27 interactions between channel shape, bed topography, and three-dimensional currents result in  
28 fine sediment settling out on bars and large sediment found in pools.

## 29 **1 Introduction**

30 Spatial variation in bed-surface sediment particle size is a common characteristic of sand-  
31 and gravel-bedded alluvial rivers (Bridge, 1977; Buffington & Montgomery, 1999; Clayton,  
32 2010; Clayton & Pitlick, 2008; Dietrich & Smith, 1984; Dietrich & Whiting, 1989; Jackson,  
33 1975; Julien & Anthony, 2002; Lisle & Madej, 1992; Nelson et al., 2010; Paola & Seal, 1995;  
34 Gary Parker & Andrews, 1985; Powell, 1998). Bed-surface sediment affects near-bed velocity  
35 and flow roughness (van Rijn, 2007), local sediment transport rates and particle mobility, (e.g.,  
36 Parker, 1990; Venditti et al., 2010; Wilcock & Crowe, 2003) and the health of riverine  
37 ecosystems (Chapman, 1988; Kondolf & Wolman, 1993; Wood & Armitage, 1997).

38 Meandering channels typically develop fine point bars on the inside of bends, and coarse  
39 pools at the outside (Bridge, 1977; Clayton, 2010; Dietrich & Whiting, 1989). Straight channels,  
40 however, develop alternating bars which exhibit coarse sediment patches located on bar tops  
41 with fine particles in the pools (Keller & Florsheim, 1993; Lanzoni, 2000; Nelson et al., 2010;  
42 Thompson et al., 1999).

43 Bed-surface sorting is the result of complex interactions between the channel planform, bed  
44 topography, the size distribution and volume of sediment supply, bed roughness due to local  
45 particle size, flow stage, and discharge. Locally nonuniform flow due to variations in planform

46 and bed morphology produces spatial variations in shear stress that may be accommodated by  
47 deposition of fine material and formation of armored patches (Dietrich & Whiting, 1989; Paola  
48 & Seal, 1995; Parker & Andrews, 1985). Bed topography also gives rise to gravitational forces  
49 facilitating cross-channel movement of particles into pools. In curved channels, counteracting  
50 forces due to secondary circular currents may overcome these gravitational forces and selectively  
51 transport finer gravel particles toward the bar (Parker & Andrews, 1985).

52 The pattern of coarse bars and fine pools in straight gravel-bed channels was investigated  
53 experimentally by Nelson et al. (2010). They observed “forced” bar topography directing flow  
54 from the bar to the pool, resulting in diverging boundary shear stress over the bar top and  
55 converging shear stress in the pool. The declining magnitude of boundary shear stress over the  
56 bar produced increasingly size-selective sediment transport, so that fine particles were  
57 preferentially transported away from the bar top and into the pool, resulting in a coarse bar and  
58 fine pool. These forced bars were spatially and temporally persistent and exerted a strong  
59 control on flow directions.

60 Detailed observations of flow and sediment transport in meandering channels have largely  
61 been constrained to sand-bedded rivers, where shear stresses are high enough that size-selective  
62 or partial sediment transport generally does not occur. In a series of studies using data from  
63 Muddy Creek, a sinuous sand-bedded alluvial stream, Dietrich (1987), Dietrich & Smith (1984),  
64 and Dietrich & Whiting (1989) performed extensive analyses of physical processes that influence  
65 the development of sorting patterns. Detailed bed load transport measurements showed that the  
66 locus of fine and coarse sediment particles cross paths downstream of the apex of the bend as a  
67 result of inward directed shear stress moving fine particles toward the bar while coarse particles  
68 tended to move toward the pool. Convective accelerations at the outside bend of the channel

69 resulted in spatially varied shear stresses that influence the trajectory of particles and contributed  
70 to the development of fine bars and coarse pools.

71       Additionally, theoretical models of sorting in bends point to the potential balance of forces  
72 due to gravity and secondary helical flow structures to develop sorting patterns. Parker &  
73 Andrews (1985) developed a theoretical model of sorting in bends that describes the forces  
74 acting on grains of varied particle sizes on the transverse slope of a bar. They state that the ratio  
75 of gravitational forces pulling sediment down to the pool to the force responsible for down and  
76 cross stream drag is greater for larger sediment particles, resulting in fine bars and coarse pools.  
77 They also developed a theoretical explanation describing the sediment transport trajectory of the  
78 coarsest sediment particles through meandering channels. Similarly, Ikeda (1989) showed that  
79 particles of greater mass more strongly feel the forces of gravity resulting in coarse pools. He  
80 also asserted that in a theoretical channel of constant curvature, sediment particles would follow  
81 a trajectory parallel to the channel centerline balanced by the transverse gravitational and  
82 opposing drag forces caused by secondary currents.

83       We generally lack detailed observations of flow, topography, sediment transport, and sorting  
84 in gravel bed meandering rivers, so it is not clear to what extent size-selective or partial sediment  
85 transport is responsible for sorting and topography in these channels, or how this interacts with  
86 the three-dimensional flow field that develops in curved channels. Dietrich et al.'s (1984, 1987,  
87 1989) observations of sediment transport and sorting in a sand-bed meander indicated that fine  
88 and coarse particles follow different trajectories through the bend, leading to the development of  
89 a fine bar and coarse pool. Here, we investigate whether the same mechanism occurs in a gravel-  
90 bed meander bend, and we hypothesize that size-selective transport may be an important control  
91 on the development of fine bars and coarse pools. In this paper we present detailed

92 measurements of topography, bed sorting patterns, the flow field, and the sediment transport  
93 field in an experimental meander bend so that we may improve our understanding of the  
94 morphodynamics of gravel-bed meandering rivers. We also explore, through detailed  
95 observation, how curvature-induced secondary flows influence sorting in a gravel-bed meander.

## 96 **2 Methods**

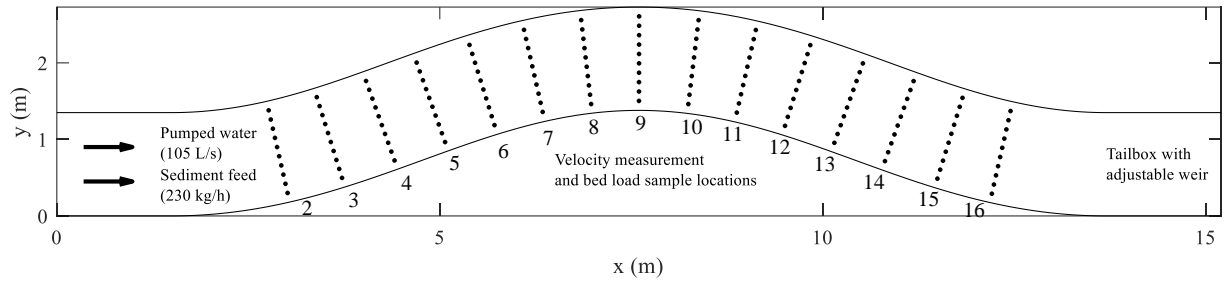
### 97 2.1 Experimental Setup

98 We conducted a flume experiment at Colorado State University's Hydraulics Laboratory in a  
99 channel with a single meander bend. The overall goal of the experiment was to develop steady-  
100 state flow, bed topography, and sorting, and then thoroughly document the flow field, sediment  
101 transport field, bed topography, and sorting patterns so that mechanisms responsible for the  
102 development of bars, pools, and sorting patterns could be discerned.

103 The flume centerline was defined by a sine-generated trace as described by Langbein &  
104 Leopold (1966):

$$\phi = \omega \sin\left(2\pi \frac{s}{m}\right) \quad (1)$$

105 where  $\phi$  is the angle of the channel centerline with respect to horizontal,  $\omega$  is the angle of  
106 departure (20 degrees in the experimental setup),  $s$  is the distance downstream along the channel  
107 centerline, and  $m$  is the meander wavelength (12.58 m in our experiment). The flume had a  
108 constant width of 1.35 m, and 1.5-m-long straight entrance and exit reaches resulting in an  
109 overall centerline of 15.58 m length (see Figure 1). The flume was initially filled with a sediment  
110 mixture to a depth of 30 cm and screeded flat to a slope of 0.007.



111

112 **Figure 1.** Flume setup schematic. 3D velocity measurements were recorded at 10 equally  
 113 spaced increments in each cross section. Bed load measurements were taken at 5 equally spaced  
 114 locations in each cross section.

115 A 40-hp pump maintained a constant water discharge of 105 L/s to the flume. The water  
 116 surface elevation at the downstream end of the flume was controlled by an adjustable tailgate to  
 117 maintain uniform conditions in the exit reach of the flume. Sediment was fed into the upstream  
 118 end of the flume with a variable-speed auger. The sediment feed rate was held constant at 230  
 119 kg/h for the duration of the experiment. Preliminary calculations using the Wilcock & Crowe  
 120 (2003) sediment transport equation indicated that this rate would be close to equilibrium  
 121 transport capacity.

122 The channel geometry, flow, and sediment feed rate were selected to achieve an average  
 123 dimensionless shear stress  $\left( \tau^* = \frac{\tau}{((\rho_s - \rho)gD_{50})} \right)$ , where  $\tau$  is the boundary shear stress,  $\rho_s$  and  $\rho$   
 124 are the densities of sediment and water,  $g$  is gravitational acceleration, and  $D_{50}$  is the median bed  
 125 sediment size) approximately twice the critical value (assumed to be  $\tau_c^* = 0.0386$ ) to produce  
 126 bar-pool morphology and transport sediment primarily as bed load. The sediment feed was  
 127 composed primarily of gravel with a mixture ranging in size from fine sand to pebbles roughly  
 128 from 0.2 mm to 8.0 mm, with a median grain size ( $D_{50}$ ) of 3.3 mm, a  $D_{84}$  of 5.0 mm, and a  $D_{16}$

129 of 1.8 mm. This range of sediment sizes was selected to ensure measurable sorting patches.  
130 Sediment exiting the downstream end of the flume was trapped in a tailbox. This sediment was  
131 dried and weighed between flume operation periods to determine the total bed load flux exiting  
132 the channel.

133 We would run the flume until the tailbox filled with sediment, typically for periods ranging  
134 from 90 to 240 minutes, at which point the flow and sediment feed would be stopped, the flume  
135 drained, and bed measurements collected as described below. We did not visually observe any  
136 significant bed changes resulting from stopping or starting the flume over the course of the  
137 experiment. The initial experimental phase of establishing quasi-equilibrium conditions, defined  
138 as conditions where the total sediment discharge was roughly equal to the sediment feed rate,  
139 lasted approximately 15 hours. Once quasi-equilibrium was achieved, the experiment continued  
140 for another ~40 hours of run time, during which detailed flow and sediment transport  
141 measurements were made as described below.

## 142 2.2 Bed load measurements

143 To characterize flow and bed load transport throughout the meander bend, we established 15  
144 cross sections along the bend oriented orthogonal to the channel centerline, with an average  
145 spacing of 0.7 m. Five bed load samples were collected at evenly spaced increments in each  
146 cross section using a Helley-Smith sampler with a 7.6 cm x 7.6 cm opening and fine mesh nylon  
147 bag. The sampler was oriented orthogonal to the cross-section, so the samples represent the  
148 downstream component of the local bed load transport vector. Sample times varied from 30 to  
149 120 seconds depending on the local rate of sediment transport. Areas where little sediment  
150 transport was observed, such as bar tops, required longer sampling times to capture enough  
151 sediment particles for analysis. A large sediment sample time is desirable when analyzing

152 transport by size fraction (Bunte & Abt, 2001). We found, however, that holding the sampler on  
153 the bed longer than 120 seconds in areas where sediment transport was low resulted in small  
154 scour features around the sampler. To minimize impact to bed topography while maximizing  
155 sample size, we found it necessary to stop bed load measurements when slight sampling-induced  
156 topographic alterations appeared. Because of this, smaller sample times are a likely factor in the  
157 variation of total measured sediment transport between cross sections. Each sediment sample  
158 was then dried, sieved and used to assess the sediment transport by size fraction throughout the  
159 channel. Total downstream sediment transport at each section was calculated by integrating the  
160 bed load samples over the width of the channel.

#### 161 2.2.1 Calculation of cross-stream bed load transport rates

162 As in prior studies where downstream sediment transport rates have been measured under  
163 quasi-equilibrium conditions (Dietrich & Smith, 1984; Nelson et al., 2010), we used sediment  
164 continuity and an assumption of steady state conditions to calculate cross-stream bed load  
165 transport rates. We first normalized the magnitude of the downstream bed load samples so that  
166 the integrated transport at each cross section was the mean value. The coefficient of variation for  
167 the total bed load transport measurements was 0.3, which is similar to values reported in other  
168 studies (0.25 at Muddy Creek (Dietrich and Smith, 1984), and 0.2 at St. Anthony Falls  
169 Laboratory (Nelson et al., 2010)). These normalized downstream transport rates were then used  
170 to compute cross-stream rates as described below.

171 Following Smith and McLean (1984) the sediment continuity equation in an orthogonal  
172 curvilinear coordinate system can be written:

$$\frac{1}{1-N} \frac{\partial q_s}{\partial s} - \frac{q_n}{(1-N)R} + \frac{\partial q_n}{\partial n} = -(1-p) \frac{\partial \eta}{\partial t} \quad (2)$$

173 where  $q_s$  is the streamwise unit sediment discharge,  $q_n$  is the cross-stream unit sediment  
 174 discharge,  $N$  is a metrical coefficient defined as  $n/R$ ,  $n$  is the normal distance from the channel  
 175 centerline (positive to the left bank),  $R$  is the local radius of curvature of the channel centerline,  $s$   
 176 is the streamwise distance downstream,  $p$  is the sediment porosity,  $\eta$  is the bed elevation, and  $t$  is  
 177 time. Under quasi-equilibrium conditions, the bed height,  $\eta$ , remains constant and therefore the  
 178 right side of the equation becomes zero. Equation 2 can then be solved by establishing a  
 179 boundary condition of  $q_n = 0$  at the right bank, (at  $n = -w/2$ , where  $w$  is the channel width).  
 180 This yields an expression for  $q_n$ :

$$q_n = -\frac{1}{1-N} \int_{-w/2}^n \frac{\partial q_s}{\partial s} dn \quad (3)$$

181 This relation can be applied for each size class in the grain-size distribution to compute size-  
 182 specific cross-stream bed load transport rates. We discretized this function to calculate  $q_n$  for all  
 183 size classes at each bed load sampling location from the second cross section downstream. The  
 184 derivatives of  $q_s$  were approximated as forward differences, so that the first calculated values of  
 185  $q_n$  were in the second cross section where sediment transport measurements were taken.

## 186 2.2 Topography measurements

187 Bed topography was measured throughout the experiment using structure-from-motion (SfM)  
 188 photogrammetry. During periods when the flow was shut down and the bed load trap was  
 189 emptied, we photographed the bed with an 18-megapixel Canon Rebel T3i digital SLR camera  
 190 with an 18-55 mm lens (typically set to a focal length of 25 mm) mounted to a tripod system that  
 191 was connected to a rolling cart that moved up and down the length of the flume. The camera was

192 oriented approximately 1.5 meters above and orthogonal to the bed. Photos were taken at  
193 approximately 0.2 m increments across the channel and in the downstream direction. The photos  
194 were taken with roughly 70% overlap to increase the accuracy of the image processing. Between  
195 flume run times, up until equilibrium bed conditions were reached, approximately 250 photos  
196 were taken and used to develop three-dimensional topographic point clouds using Agisoft  
197 Metashape, and once equilibrium bed conditions were reached, 550 photos were used to develop  
198 a higher-resolution point cloud with less than 0.5 mm point spacing. Photos were taken in JPEG  
199 file format for compatibility with MetaShape. The following workflow was followed to generate  
200 a dense point cloud in Metashape: 1) Import images to the software and align with ‘high’  
201 accuracy; 2) Identify ground targets at locations surveyed prior to the flume run; 3) Optimize  
202 images and camera locations; 4) Generate dense point cloud with ‘high’ quality. The dense point  
203 cloud generated in Metashape was opened in CloudCompare where equilibrium bed conditions  
204 were evaluated by comparing sequential point clouds. Bed elevation changes beyond  $t = 15$   
205 hours were negligible. In CloudCompare, a polyline of the flume planform geometry was used to  
206 clip the unnecessary point data, and the data were then resampled to 5 mm spacing to reduce  
207 processing times.

208 After bed load and flow velocity measurements were taken and prior to the collection of  
209 photos for the high-resolution SfM point cloud, the sediment feed and flow were shut off while  
210 simultaneously raising a downstream weir on the tailbox. The increased downstream water  
211 surface elevation and halted flow resulted in negligible flow velocities in the channel as the  
212 flume drained slowly, preserving the topography of the bed.

213 The SfM point clouds were interpolated onto a rectilinear grid with spacing of 0.01 m using a  
214 kriging algorithm in Golden Software’s Surfer program. Cells that fell outside the flume

215 boundaries were assigned NODATA values. For the purpose of comparing bed surface elevation  
216 after each flume run, the average value at each longitudinal gridded increment (y values,  
217 ignoring cells containing NODATA) was calculated and plotted as a function of horizontal  
218 distance downstream (the incremental grid number (x index) multiplied by 0.01 m). A detrended  
219 topographic bed elevation map was generated by calculating the mean downstream Cartesian  
220 slope over the channel length and offsetting the gridded increments in each column (y values)  
221 such that the mean elevation at each column was equal.

### 222 2.3 Sorting measurement

223 Sediment sorting patterns were mapped by visual observation following the method  
224 described by Nelson et al. (2009) and Nelson et al. (2010). The bed was divided into 5 facies, or  
225 patch types based on a visual assessment of the local average grain size and degree of sorting.  
226 Grain-size distributions for each patch type were measured noninvasively using digital  
227 photographs. Photos were taken orthogonal to the surface of the bed in each patch type,  
228 capturing an area approximately 25 by 40 cm. Each photo was opened in MATLAB and divided  
229 into an equally spaced grid of 100 points. The intermediate axis of the particle at each grid  
230 intersection point was measured by drawing a line across the particle. A steel ball bearing 3.175  
231 mm in diameter was placed in each of the photos as a reference to determine scale of each  
232 photograph; this scale was used to convert the measured sediment diameters from pixels to  
233 millimeters.

### 234 2.4 Velocity measurement

235 Velocity, water surface elevation, and bed elevation measurements were taken approximately  
236 simultaneously at 10 equally spaced points in each of the 15 cross sections as seen in Figure 1.

237 Water surface elevations were measured with a point gauge and referenced to the local  
238 coordinate system. A side-looking Nortek Vectrino+ acoustic Doppler velocimeter (ADV) was  
239 used to measure three-dimensional flow velocities near the water surface and in shallow areas  
240 such as over the bar top. ADV measurements were collected at a frequency of 100 Hz over 30  
241 seconds. In areas of flow deeper than 8 cm, velocity profiles were collected using a downward-  
242 looking Nortek Vectrino Profiler, a profiling acoustic Doppler velocimeter (P-ADV). The P-  
243 ADV measures three-dimensional velocity at 100 Hz in thirty 1-mm-high bins spanning a 3 cm  
244 vertical window. In areas where flow depth exceeded 10 cm, multiple, stacked, 3-cm velocity  
245 profiles were captured with the P-ADV, measuring as much of the water column as possible. Bed  
246 elevations were measured using a point gauge immediately prior to the velocity measurements.  
247 The P-ADV is also capable of measuring the depth from the sensor to the bed. In our analysis,  
248 the P-ADV-measured bed elevation was used and verified with the point gauge reading.

249 The velocity measurements were plotted in MATLAB with isoline-generated contour plots  
250 overlain by vectors representing the cross stream and vertical velocity components. This was  
251 done for all cross sections where velocity measurements were taken.

## 252 2.5 Shear stress calculations

253 We used the velocity profiles to calculate boundary shear stress throughout the channel by  
254 fitting a logarithmic function to the near-bed portion of the velocity profile (Wilcock, 1996,  
255 Yager et al., 2018). A logarithmic velocity profile is expressed mathematically through the law  
256 of the wall:

257

$$u(z) = \frac{u_*}{\kappa} \ln\left(\frac{z}{z_0}\right) \quad (4)$$

258 where  $u(z)$  is the velocity at the height above the bed  $z$ ,  $u_*$  is the shear velocity, defined as  $u_* \equiv$   
 259  $\sqrt{\tau/\rho}$ , where  $\tau$  is the boundary shear stress and  $\rho$  is the water density,  $z_0$  is the roughness height  
 260 above the bed where  $u(z) = 0$ , and  $\kappa = 0.4$  is von Karman's constant.

261 The velocity  $u(z)$  is the resultant of measured downstream and cross-stream components of  
 262 the velocity

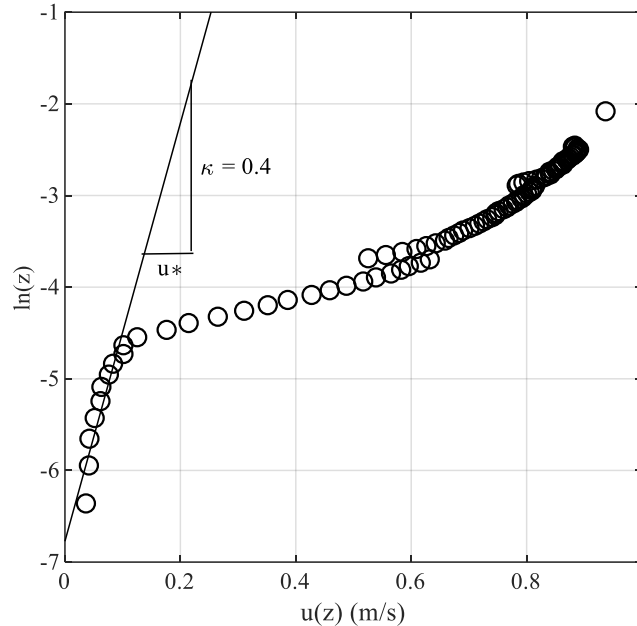
$$u(z) = \sqrt{|u_s(z)|^2 + |u_n(z)|^2} \quad (5)$$

263 where  $u_s$  is the local average streamwise measured velocity and  $u_n$  is the local average measured  
 264 transverse velocity. The measured velocity profiles were assessed using guidelines suggested in  
 265 Wilcock (1996), such that logarithmic profiles should be present where  $3D_{84} < z < h/5$  and  
 266  $h/D_{84} > 15$ . For each of the 150 measured velocity profiles, we plotted  $u(z)$  vs  $\ln(z)$  and  
 267 identified regions that met the criteria and followed a clear linear trend (see Figure 2). Equation 4  
 268 can be rewritten as

$$\ln(z) = \frac{\kappa}{u_*} u(z) + \ln(z_0) \quad (6)$$

269 so that the slope of a linear regression of  $\ln(z)$  vs.  $u(z)$  corresponds to  $\kappa/u_*$ , yielding an  
 270 estimate of the shear velocity and therefore the boundary shear stress. In some locations the flow  
 271 depth was too shallow to measure full velocity profiles. In these areas, we measured near-surface  
 272 and near-bed velocities with the side-looking Vectrino ADV. As described by Dietrich and  
 273 Whiting (1989) and Nelson et al. (2010), we estimated shear stress at these locations with a  
 274 single velocity measurement. Here, equation (6) was still used, and we used the local bed surface

275 grain-size distribution to estimate the roughness height  $z_0 = 0.1D_{84}$  (Dietrich & Whiting, 1989;  
 276 Leopold & Wolman, 1957).



277  
 278 **Figure 2.** Stacked measured velocity profile showing the logarithmic relation of flow depth to  
 279 velocity near the bed in a patch of fine sediment particles. At a height above the bed of  
 280 approximately 0.012 m ( $\ln(z) = -4.4$ ), the profile diverges from the logarithmic relationship, so  
 281 only the near-bed values are used to compute shear stress. The line shows the linear fit to the  
 282 near-bed profile.

283

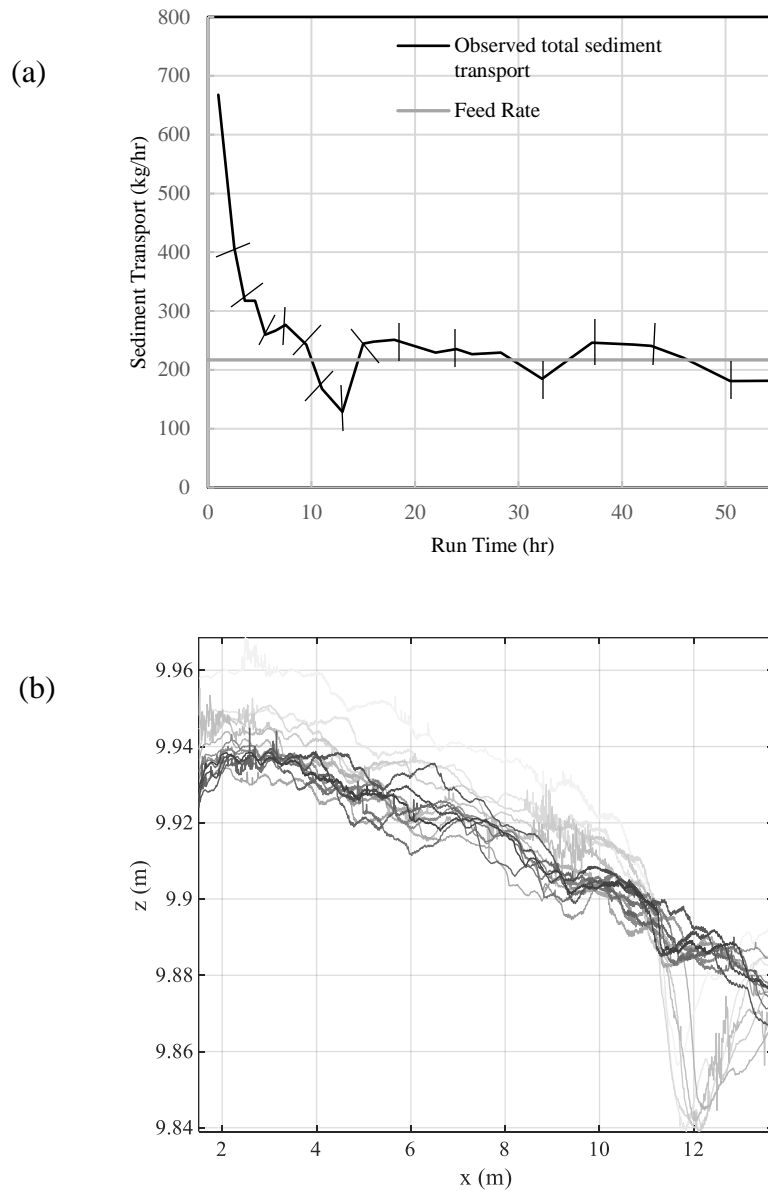
### 284 3. Results

#### 285 3.1 Equilibrium topography

286 Sediment transport exiting the flume was initially much higher than the feed rate, exceeding  
 287 600 kg/h (Figure 3a). The high initial sediment transport rate reflects about 6 cm of scour that

288 occurred at the downstream end of the flume (Figure 3b) and subsequent erosion of the upstream  
289 half of the flume bed as the slope relaxed from its initial value of 0.007 to a quasi-equilibrium  
290 value of 0.005. After 15 hours of run time, sediment transport at the flume outlet was  
291 approximately equal to the sediment feed rate (Figure 3a) and the bed profile became generally  
292 unchanging (Figure 3b).

293 Equilibrium bed topography was characterized by point bars that developed on the left side  
294 of the channel upstream of the bend apex and on the right side of the channel downstream of the  
295 bend apex, and adjacent pools along the opposite sides of the channel (Figure 4). Due to the  
296 restricted length of the basin in which the flume was constructed, conditions at the upstream end  
297 of the bend did not become fully developed. The relief between the bar and pool upstream of the  
298 bend apex was approximately 15 cm, and the relief downstream of the apex was about 25 cm.  
299 Because of likely entrance effects, we focus our analysis of bed topography and sorting on the  
300 region downstream of the bend apex ( $x = 7$  m in Figure 4).



301

302

**Figure 3.** (a) Measured sediment transport rate as defined by dry weight of sediment in the tail

303

box over flume run time contributing to the tailbox sample. The tick marks intersect the curve

304

where bed topography was measured. (b) Bed elevation and evolution of a quasi-equilibrium

305

conditions. The lines grow increasingly dark with flume run time at each bed topography

306

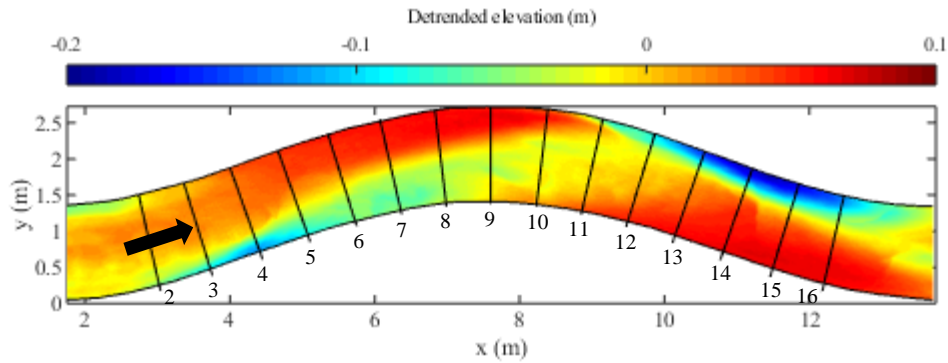
measurement and correspond to the flume run time of tick marks in Figure 3a. Notice that the

307

darkest lines converge to a state of roughly equal slope throughout the channel, and tend to

308

change very little with time.



309

310 **Figure 4.** Detrended equilibrium bed topography. Cool shaded areas are topographically low  
 311 (pools) and warm shaded areas are topographically high (point bar).

312 3.2 Sorting

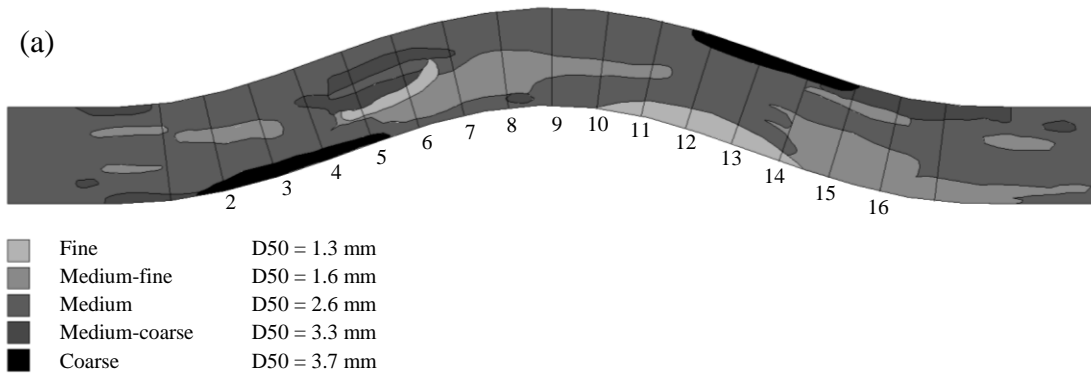
313 The sorting pattern observed under quasi-equilibrium conditions is shown in Figure 5a. The  
 314 bed was categorized into five patch types, and the grain-size distributions of these patch types are  
 315 presented in Figure 5b. Upstream of the bend apex, longitudinal patches of medium-fine  
 316 sediment developed, which probably resulted from flow over cinderblocks placed at the  
 317 upstream entrance to the flume to dissipate energy and prevent upstream scour. There were one-  
 318 to two-inch spaces between the blocks where flow passed through and affected the topography  
 319 and sorting patterns until just upstream of the bend apex. Where flows were deflected as the  
 320 curvature of the planform increased, there was a patch of coarse particles ( $D_{50} = 3.7$  mm) that is  
 321 consistent with observations made at the other pool in the channel and in other studies.

322 The point bar downstream of the bend apex exhibited a downstream fining pattern, with  
 323 medium sediment ( $D_{50} = 2.6$  mm) at the apex of the bend transitioning to fine sediment ( $D_{50} =$   
 324 1.3 mm) roughly one meter downstream, which in turn transitioned to medium-fine particles ( $D_{50} =$   
 325 1.6 mm) further downstream.

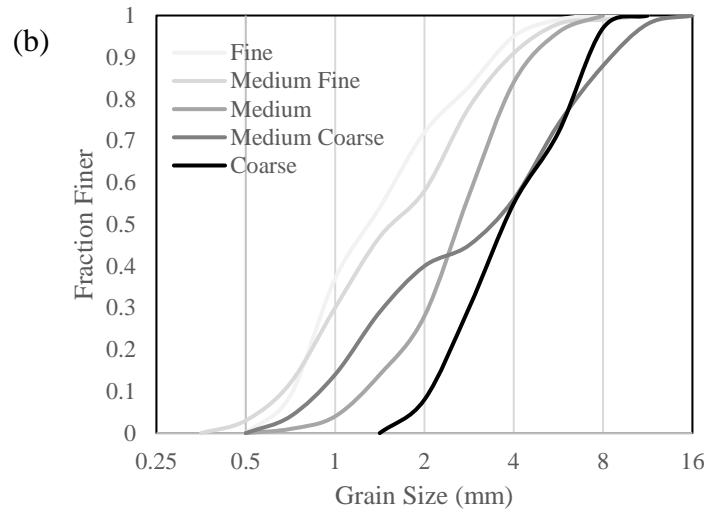
326 At the outside bend, a coarse sediment patch located in the pool extended approximately 2  
327 meters along the channel edge. The bed then becomes increasingly fine, transitioning to a  
328 medium-coarse patch, and further downstream to medium. A small medium-fine patch is located  
329 adjacent to the coarse pool, which may be the result of selective transport as secondary currents  
330 are strongly developed at this location.

331 At the apex, in the center of the channel, a ribbon of medium-fine bed material extends  
332 downstream, eventually transitioning to medium. Topographically, this is located at the front of  
333 the bar. A unique bimodal distribution was found in the medium-coarse patch located  
334 downstream of the pool at the outside bend. However, the  $D_{50}$  here did fall between those of the  
335 coarse and medium facies types.

336



337



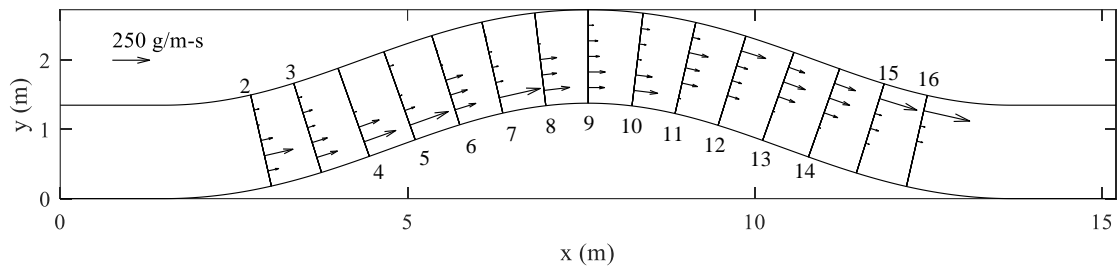
338

339 **Figure 5.** (a) Sediment sorting pattern observed at equilibrium bed topography. A fine patch  
 340 developed downstream of the bend apex on the inside of the curve. A clear coarse patch  
 341 developed at the outside of curve in the pool. (b) Grain-size distributions for each facies type.

342 The bimodal medium-coarse patch was located just downstream of the pool.

### 343 3.3 Bed load transport

344 Bed load transport measurements collected under quasi-equilibrium are depicted in Figure 6.  
 345 The locus of maximum transport shifts from the inside to the outside edge of the channel a short  
 346 distance downstream of the bend apex. When comparing patterns of sorted patches, it is useful to  
 347 identify locations where total normalized bed load transport changes dramatically in similar cross  
 348 section stations. Perhaps the most drastic example of this behavior is seen at cross sections 10  
 349 and 11, where the total unit bed load transport near the inside edge of the channel drops from  
 350 0.16 kg/m/s to 0.014 kg/m/s. It is at this same location that the bed sorting pattern shifts from  
 351 medium ( $D_{50} = 2.6$  mm), to fine ( $D_{50} = 1.3$ mm). The sediment transport near the outside bend at  
 352 cross sections 11 and 12 shows a sharp increase, rising from 0.05 kg/m/s to 0.17 kg/m/s in this  
 353 location, the sorting pattern shifts from medium ( $D_{50} = 2.6$  mm) to coarse ( $D_{50} = 3.7$  mm).



354

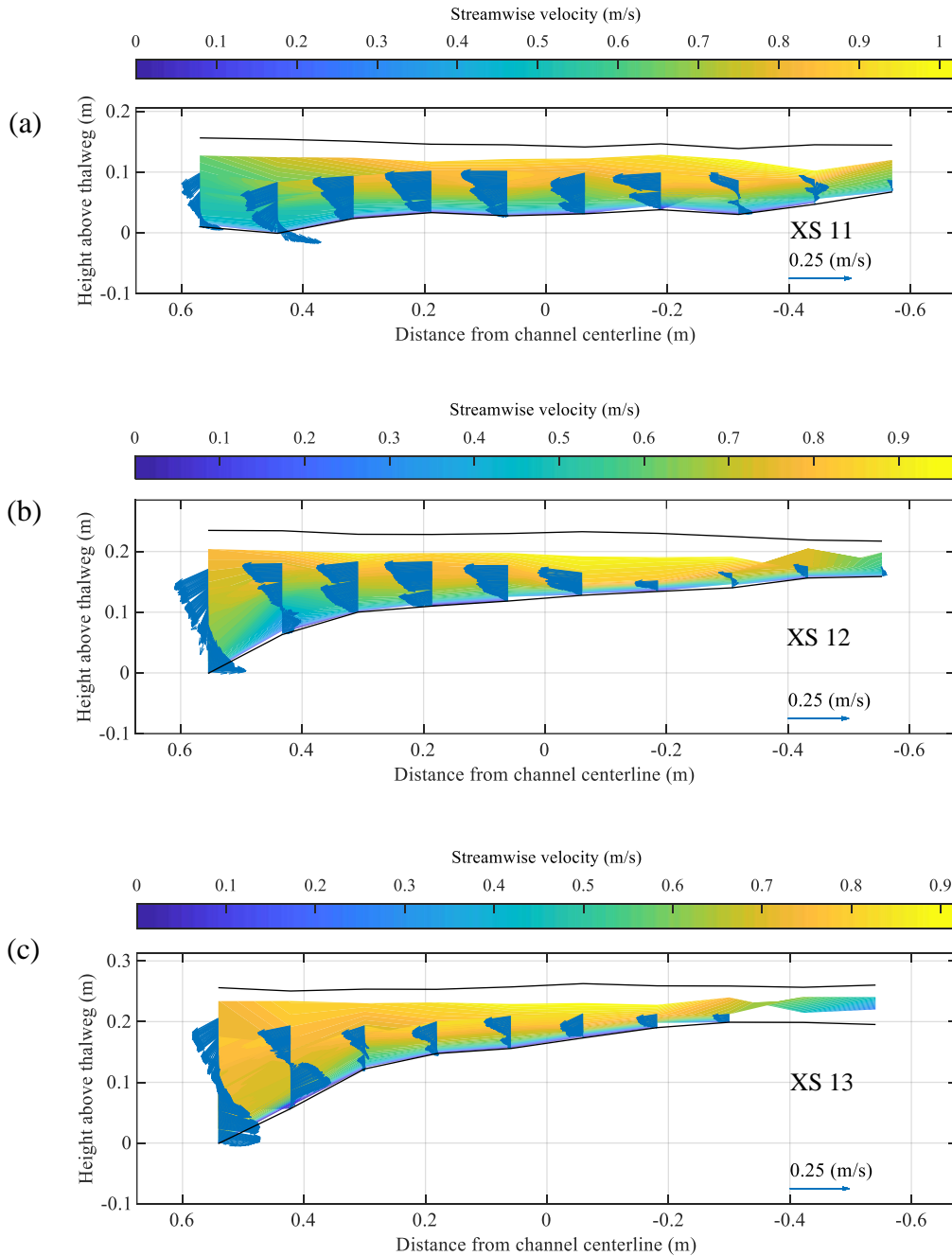
355 **Figure 6.** Magnitude of unit bed load samples measured through the flume. The region of high  
 356 bed load transport shifts from one side of the channel to the other downstream of the bend apex.

357 Figures 9b and c depict vectors of sediment transport for fine sediment (finer than 2 mm,  
 358 Figure 9b), and coarse sediment (coarser than 4 mm, Figure 9c), where the cross-stream  
 359 components of the transport vectors were computed using the continuity equation as described in  
 360 Section 2.2.1. In general, both coarse and fine particle trajectories are slightly oriented toward  
 361 the left bank at cross sections 10, 11, and 12, and shift toward the right bank at cross sections 14,  
 362 15, and 16. Interestingly though, at cross section 13, the coarse particles display a downstream  
 363 trajectory, where fine particles show a shift to the right.

### 364 3.4 Velocity flow field and secondary currents

365 Figure 7 shows the measured three-dimensional velocity field downstream of the bend apex  
 366 (cross section 11) to the downstream pool (cross section 13). Near the bend apex (cross section  
 367 11), the high-velocity core was on the right side of the channel, with flow laterally oriented  
 368 toward the left bank almost everywhere. There are indications, however, of small secondary  
 369 currents on the inside bend, likely caused by the turbulent fluctuations in flow that develop in the  
 370 shadow of the channel curve.

371 Moving downstream, the high-velocity core begins to shift to the left side of the channel over  
372 the developing pool (cross section 13), and a well-developed secondary circulation with near-bed  
373 flow directed toward the inner bank of the bend. The secondary circulation is confined to a fairly  
374 small portion of the total channel width until 3 meters downstream of the bend apex at cross  
375 section 14. Not until cross-section 15 do the secondary circular currents send near-bed flows past  
376 the channel centerline and onto the bar on the right side of the channel.



377

378

379

380 **Figure 7.** Cross sectional plots of 3D velocity measurements taken at cross sections 11, 12, 13.

381 The aquamarine blue to yellow heatmap represents the magnitude of the streamwise velocity.

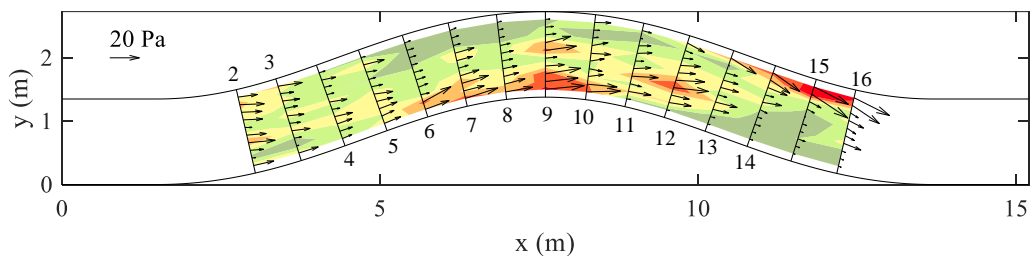
382 The blue arrow vectors represent the transverse and vertical components of the velocity

383 measurements taken at 1 mm increments through the water column. There is a lack of data near

384 the water surface, because the Vectrino Profiler P-ADV required full submergence to function  
 385 properly. The near-surface velocity values were supplemented with measurements taken by a  
 386 single point velocimeter that required less submergence.

387 Shear stress field

388  
 389 Figure 8 shows the boundary shear stress vector field computed from the velocity  
 390 measurements overlaid on a shear stress contour map generated using the MATLAB contour  
 391 function, which projects interpolated values between measurement points on a grid. The stress  
 392 vectors share the same direction as near-bed velocity. The region of maximum shear stress shifts  
 393 from the inside to outside of the bend past its apex. From cross-section 9 to 10, stress drops to  
 394 almost zero at the same location where the finest sorting patch begins (Figure 6a).



395  
 396 **Figure 8.** Boundary shear stress calculated from near-bed velocities. The region of high  
 397 shear stress shifts from inside to outside past the bend apex. The shear stress in the upper half  
 398 of the pool is low where a patch of coarse sediment was found. Shear stress vectors converge  
 399 where the lateral slope in topography is greatest near the pool.

400 **4. Discussion**

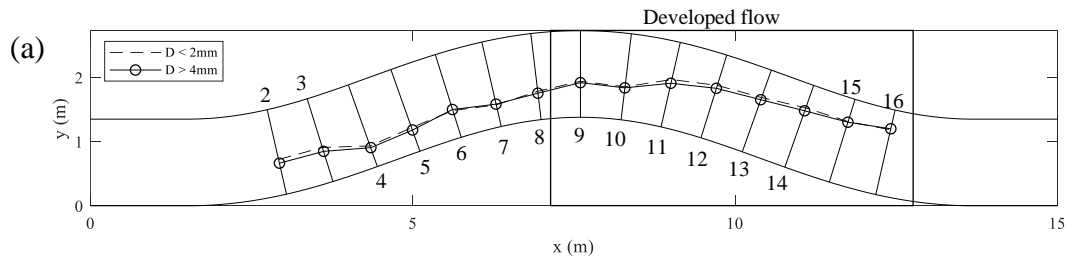
401 4.1 Selective transport and sorting in gravel vs. sand-bed meanders

402 The ratio of cross-stream ( $q_n$ ) to downstream ( $q_s$ ) unit sediment transport, averaged across  
403 each cross section, for fine (< 2 mm) and coarse (> 4 mm) particles is presented in Figure 9d. At  
404 cross section 13 (8.5 m downstream), the sediment particles finer than 2 mm shift from an  
405 outward trajectory (toward the pool) to inward (toward the bar). In this region downstream of the  
406 apex at the inside bank, shear stress decreases from 23 to 2 Pa (see Figure 8), and the transport  
407 becomes size-selective with mostly fine particles moving.

408 The percentage of total unit transport represented by fine particles (< 2 mm) increases over  
409 the bar top, from 3% at cross section 10 to 11% at cross section 11 and then 24% at cross section  
410 12, while the percentage of total transport of coarse particles (> 4 mm) decreases from 15% at  
411 cross section 9 down to 6% by cross section 13 and drops below 3% in cross sections 14 and 15.  
412 Dietrich and Whiting (1989) observed a similar occurrence of selective fine sediment transport  
413 on the bar although the data collected at Rio Grande del Ranchos River were sparse. They  
414 suggested that if available, sand may be thrown into suspension in the zone of maximum shear  
415 stress at the upstream part of the bend and settle down to travel as bed load over the bar top. We  
416 observed transport of fine particles (including sand size) as bed load through the entire bend.  
417 Their observations and ours suggest that the divergence of shear stress on the bar top is  
418 accommodated by selective transport and deposition of fine material.

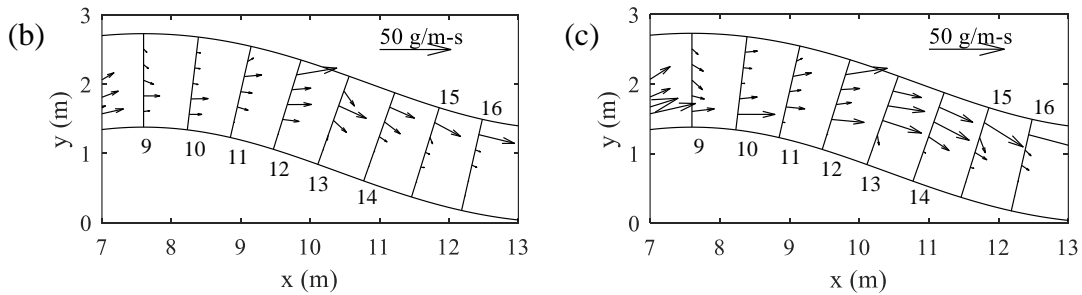
419 From cross sections 12 through 15, the  $q_n/q_s$  ratio for fine sediment drops rapidly and  
420 remains negative. At cross section 13, the near-bed inward directed flow extends far enough into  
421 the channel that effects are felt strongly by small particles. The  $q_n/q_s$  ratio for coarse sediment  
422 also transitions but not until cross section 14 does it become negative indicating an overall  
423 trajectory to the right bank. This delayed reaction by the coarse particles suggests selective cross  
424 stream transport of fine particles resulting in coarser pools.

425 Although there are noticeable local differences in the transport trajectories of different sized  
 426 particles, the loci of maximum transport of large ( $>4$  mm) and fine ( $<2$  mm) particles are nearly  
 427 identical (Figure 9a). In their studies of sediment transport through a sand-bedded meander bend,  
 428 Dietrich and Whiting (1989) noticed a drastic difference in the trajectories of a range of particle  
 429 sizes.

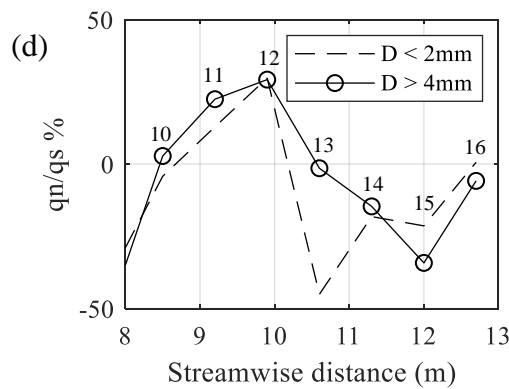


430

431



432



433

434

435 **Figure 9** (a) Locus of maximum transport of particles finer than 2 mm and coarser than 4 mm (b)  
436 Vectors showing direction and magnitude of unit sediment discharge of particles finer than 2 mm  
437 in the region of developed flow. (c) Vectors showing direction and magnitude of unit sediment  
438 discharge of particles coarser than 4 mm in the region of developed flow. (d) Ratio of transverse  
439 to streamwise unit sediment flux for particles coarse and fine particles. A positive  $q_n/q_s$  ratio  
440 indicates a trajectory toward the left bank and negative to the right.

441 In their experiment the finest and coarsest class of particles measured moved through the  
442 bend out of phase, crossing paths a short distance downstream of the bend apex. This marked  
443 difference likely indicates that, although present, varied cross-stream transport by size fraction in  
444 gravel is not as significant when producing equilibrium bed topography or roughness patches as  
445 it is in sand bedded channels. This is affirmed by observations of helical flows and analysis of  
446 Shields stresses. It should be noted that compared to our flume, the sand-bed study had a smaller  
447 radius of curvature and a greater maximum angle of departure influencing the strength of helical  
448 flows and possibly sediment trajectories.

449 To investigate the possibility that the sorting patterns we observed were at least in part a  
450 result of partial or selective transport, we used the shear stress field calculated from our velocity  
451 observations to estimate where particles of different size should be mobile, by calculating the  
452 dimensionless shear stress ( $\tau^*$ ) and comparing that to a critical value ( $\tau^*_c$ , taken here to be  
453 0.0386; Parker, 1990). Figure 10 shows regions where the dimensionless stress for 2 mm, 4 mm,  
454 and 8 mm sediment exceeds or falls below the critical value, expressed as the stress ratio  $\tau^*/\tau^*_c$ .  
455 The stress ratio is well below 1 for 4 mm sediment particles where the finest patch was located,  
456 at the inside of the channel, just downstream of the bend apex. For 2 mm diameter particles, the  
457 stress ratio remains well above 1 throughout nearly the entire channel. This indicates that the

458 coarse sediment particles were not fully mobile at all points in the channel, but the fine particles  
459 were. The stress ratio for 8 mm particles was less than 1 in the upstream half of the pool but was  
460 generally greater than 1 for all smaller particles. Sediment particles larger than 8 mm in diameter  
461 made up less than 2% by weight of the sediment mixture fed into the flume. In the region of  
462 developed flow (downstream of the apex) they were only found in significant numbers in the  
463 deepest part of the pool. This suggests that these large particles armored the pool with fine  
464 particles selectively transported inward, upslope to the region of maximum shear stress.

465

466

467

468

469

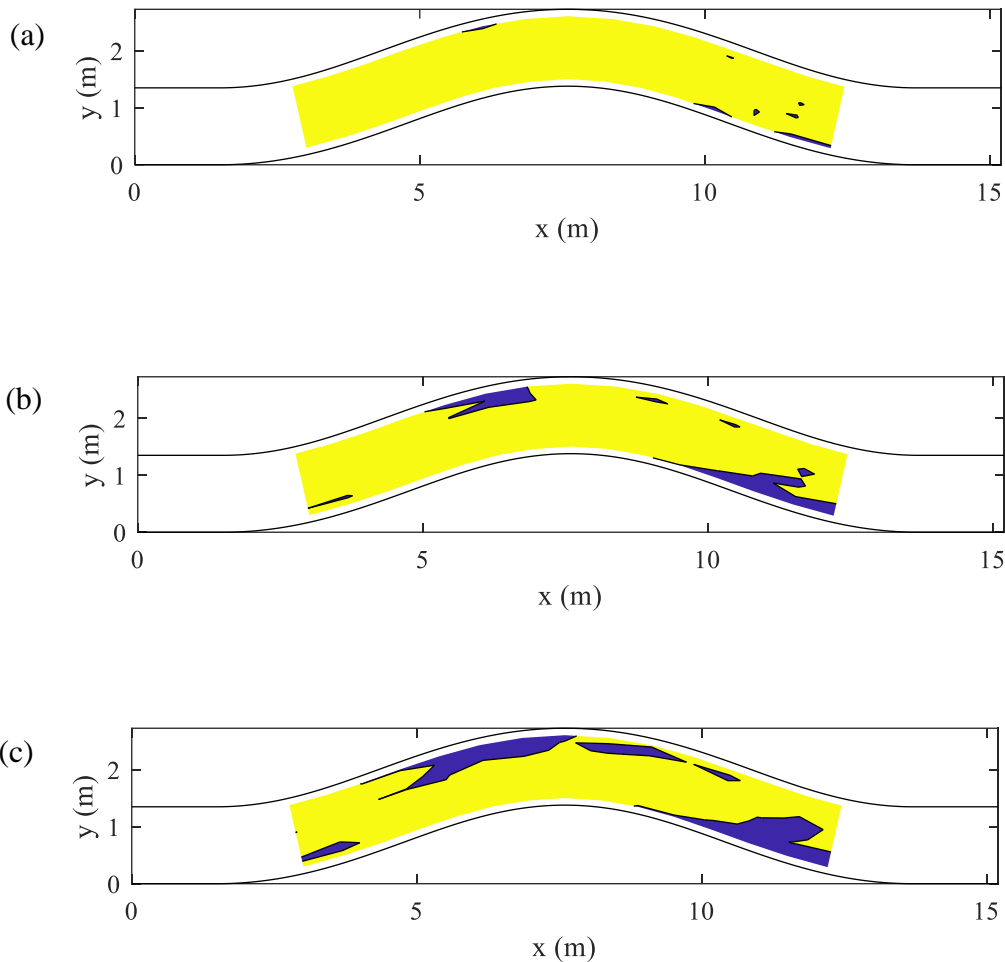
470

471

472

473

474



475

476

477

478 **Figure 10.** (a)  $\tau^*/\tau_c^*$  for 2 mm sediment is represented where the blue shaded regions represent a  
 479 ratio less than 1 and the yellow shaded regions, greater than one. At almost all points in the  
 480 channel, the Shields to reference Shields stress ratio is greater than 1. Particles finer than 2 mm  
 481 are expected to be mobile throughout the channel. (b)  $\tau^*/\tau_c^*$  for 4 mm sediment; on the bar tops,  
 482 the ratio exceeds 1 for particles coarser than 4mm, and therefore, particles larger than 4 mm are  
 483 unlikely to be transported onto the bar. (c)  $\tau^*/\tau_c^*$  for 8 mm sediment; in the upstream half of the  
 484 pool, the ratio is below zero. This indicates that as coarse particles are transported toward the  
 485 pool, they will remain there while finer sediment particles are selectively transported through the  
 486 pool.

487 4.2 Gravity verses secondary flows

488       Near the outside edge of the bend calculated shear stress vectors indicate that there is flow  
489 convergence along the edge of the pool. This convergent flow corresponds with the transition  
490 from the coarsest observed bed load patch ( $D_{50} = 3.6$  mm) to a medium patch ( $D_{50} = 2.3$  mm).  
491 The shear stress magnitude in upper half of the pool is not high compared to the other regions in  
492 the channel. The shear stress in the pool does not increase with sediment size, indicating that  
493 selective transport of fine particles by secondary currents plays an important role in the  
494 development of coarsest patches. The largest particles ( $> 8$  mm) were only observed in the pools,  
495 probably because the strong gravitational forces on the side slope of the bar were greater than  
496 upslope forces from secondary currents. The secondary currents were confined to the deepest  
497 part of the upstream half of the pool and effectively shunted smaller particles inward laterally  
498 upslope toward the zone of maximum shear stress where the bar transitions to the pool.

499       In the patch of finest sediment particles ( $D_{50} = 1.5$  mm) past the bend apex, there is a very  
500 low lateral slope. The average lateral slope for cross sections 12 and 13 in the fines patch was  
501 0.2% compared to an average slope through the whole cross section of 20%. This leads us to  
502 conclude that gravitational forces associated with particles rolling toward the pool have little  
503 effect here. A divergence of both shear stress and sediment transport is the controlling factor in  
504 the deposition of fine particles on the bar. Near the pool, however, the flat bar top transitions to a  
505 steep slope into the pool where both the effects of gravity and secondary currents are present.  
506 Coarse particles were found in the pool, having been more strongly affected by gravitational  
507 forces than the inward-directed near bed velocity. There is a shortage of investigations into the  
508 effects that varied degrees of meandering and other planform geometry have on the extent of  
509 secondary currents and their influence on sorting of both sand and gravel beds. A study of this

510 nature would prove meaningful in identifying thresholds at which certain mechanisms for sorting  
511 are strongest.

## 512 **5. Conclusion**

513 To our knowledge, this study involving coupled observations of bed load transport by size  
514 fraction, near-bed velocity, calculated shear stress, and quasi-equilibrium bed topography leading  
515 to clearly sorted patches is the first of its kind in a gravel-bed meandering channel. We were able  
516 to measure each element at high resolution due to the controlled flume environment. In our  
517 experiment, spatial variations in shear stress led to conditions where, locally, coarser fractions of  
518 the grain-size distribution could become immobile, and this development of partial and selective  
519 transport is primarily responsible for the persistence of coarse pools and fine bars. This contrasts  
520 with sand-bedded meandering channels, where generally all particle sizes are fully mobile and  
521 sorting is more dependent on the balance of secondary flows and gravitational effects. We show  
522 that although the trajectories of coarse and fine particles are varied in localized regions of the  
523 meander bend, the maximum transport of all particle sizes occurs in the corridor of greatest shear  
524 stress, which was also different from observations in a sand-bedded channel. In pools, secondary  
525 currents produce near-bed, upslope shear that counteracts gravitational forces. The effects of this  
526 secondary flow were constrained to the deepest part of the pool and coarsest sorted patch until  
527 well past the bend apex. Extent of secondary currents and their influence on sorting is a function  
528 of planform geometry. These observed mechanisms suggest that divergence in boundary shear  
529 stress is accommodated by spatially varied preferential bed load transport, resulting in persistent  
530 sorted patches of varying degrees of roughness and equilibrium conditions.

531

532 **Acknowledgments**

533 We thank Ryan Brown, and David Cortese for their help with data collection. Financial support  
534 for this research was provided by the National Science Foundation award EAR-1455259

535 **Open Research**

536 Data associated with this study can be accessed from the Colorado State University Digital  
537 Repository and can be accessed here <http://dx.doi.org/10.25675/10217/234139>

## References

- Bridge, J. S. (1977). Flow, bed topography, grain size and sedimentary structure in open channel bends: A three-dimensional model. *Earth Surface Processes*, 2(4), 401–416.  
<https://doi.org/10.1002/esp.3290020410>
- Buffington, J. M., & Montgomery, D. R. (1999). A Procedure for classifying textural facies in gravel-bed rivers. *Water Resour. Res.*, 35(6), 1903–1914.  
<https://doi.org/10.1029/1999WR900041>
- Bunte, K., & Abt, S. R. (2001). Sampling surface and subsurface particle-size distributions in wadable gravel-and cobble-bed streams for analyses in sediment transport, hydraulics, and streambed monitoring. *Gen. Tech. Rep. RMRS-GTR-74. Fort Collins, CO: U.S. Department of Agriculture, Forest Service, Rocky Mountain Research Station. 428 p., 74.*  
<https://doi.org/10.2737/RMRS-GTR-74>
- Chapman, D. W. (1988). Critical Review of Variables Used to Define Effects of Fines in Redds of Large Salmonids. *Transactions of the American Fisheries Society*, 117(1), 1–21.  
[https://doi.org/10.1577/1548-8659\(1988\)117<0001:CROVUT>2.3.CO;2](https://doi.org/10.1577/1548-8659(1988)117<0001:CROVUT>2.3.CO;2)
- Clayton, J. A. (2010). Local sorting, bend curvature, and particle mobility in meandering gravel bed rivers: TECHNICAL NOTE. *Water Resour. Res.*, 46(2), 371.  
<https://doi.org/10.1029/2008WR007669>
- Clayton, J. A., & Pitlick, J. (2008). Persistence of the surface texture of a gravel-bed river during a large flood. *Earth Surf. Processes Landforms*, 33(5), 661–673.  
<https://doi.org/10.1002/esp.1567>

- Dietrich, W. E. (1987). Mechanics of Flow and Sediment Transport in River Bends. In K. S. Richards (Ed.), *River Channels: environment and process* (pp. 129–158). Basil Blackwell.
- Dietrich, W. E., & Smith, J. D. (1984). Bed Load Transport in a River Meander. *Water Resources Research*, 20(10), 1355–1380. <https://doi.org/10.1029/wr020i010p01355>
- Dietrich, W. E., & Whiting, P. (1989). Boundary shear stress and sediment transport in river meanders of sand and gravel. *Water Resources Monograph*, 1–50. <https://doi.org/10.1029/wm012p0001>
- Ikeda, S. (1989). Sediment Transport and Sorting at Bends. In *River Meandering* (pp. 103–125). American Geophysical Union (AGU). <https://doi.org/10.1029/WM012p0103>
- Jackson, R. G. (1975). Velocity–bed-form–texture patterns of meander bends in the lower Wabash River of Illinois and Indiana. *GSA Bulletin*, 86(11), 1511–1522. [https://doi.org/10.1130/0016-7606\(1975\)86<1511:VPOMBI>2.0.CO;2](https://doi.org/10.1130/0016-7606(1975)86<1511:VPOMBI>2.0.CO;2)
- Julien, P. Y., & Anthony, D. J. (2002). Bed load motion and grain sorting in a meandering stream. *J. Hydraul. Res.*, 40(2), 125–133. <https://doi.org/10.1080/00221680209499855>
- Keller, E. A., & Florsheim, J. L. (1993). Velocity-reversal hypothesis: A model approach. *Earth Surf. Processes Landforms*, 18(8), 733–740. <https://doi.org/10.1002/esp.3290180807>
- Kondolf, G. M., & Wolman, M. G. (1993). The sizes of salmonid spawning gravels. *Water Resources Research*, 29(7), 2275–2285. <https://doi.org/10.1029/93WR00402>
- Langbein, W. B., & Leopold, L. B. (1966). *River meanders - Theory of minimum variance* (Professional Paper). <https://doi.org/10.3133/pp422H>
- Lanzoni, S. (2000). Experiments on bar formation in a straight flume: 2. Graded sediment. *Water Resources Research*, 36(11), 3351–3363. <https://doi.org/10.1029/2000WR900161>

Leopold, L. B., & Wolman, M. G. (1957). *River channel patterns: Braided, meandering, and straight* (USGS Numbered Series No. 282- B) (p. 50). Washington, D.C.: U.S.

Government Printing Office. Retrieved from <http://pubs.er.usgs.gov/publication/pp282B>

Lisle, T. E., & Madej, M. A. (1992). Spatial variation in armouring in a channel with high sediment supply. In *Dynamics of Gravel-bed Rivers*. London: John Wiley and Sons.

Retrieved from <https://www.fs.usda.gov/treearch/pubs/7829>

Nelson, P. A., Venditti, J. G., Dietrich, W. E., Kirchner, J. W., Ikeda, H., Iseya, F., & Sklar, L. S. (2009). Response of bed surface patchiness to reductions in sediment supply. *Journal of Geophysical Research: Earth Surface*, *114*(F2). <https://doi.org/10.1029/2008JF001144>

Nelson, P. A., Dietrich, W. E., & Venditti, J. G. (2010). Bed topography and the development of forced bed surface patches. *J. Geophys. Res.*, *115*(F4), 199.

<https://doi.org/10.1029/2010JF001747>

Paola, C., & Seal, R. (1995). Grain Size Patchiness as a Cause of Selective Deposition and Downstream Fining. *Water Resources Research*, *31*(5), 1395–1407.

<https://doi.org/10.1029/94WR02975>

Parker, G. (1990). Surface-based bedload transport relation for gravel rivers. *Journal of Hydraulic Research*, *28*(4), 417–436. <https://doi.org/10.1080/00221689009499058>

Parker, Gary, & Andrews, E. D. (1985). Sorting of Bed Load Sediment by Flow in Meander Bends. *Water Resources Research*, *21*(9), 1361–1373.

<https://doi.org/10.1029/wr021i009p01361>

Powell, D. M. (1998). Patterns and processes of sediment sorting in gravel-bed rivers. *Progress in Physical Geography: Earth and Environment*, *22*(1), 1–32.

<https://doi.org/10.1177/030913339802200101>

- Smith, J. D., & Mclean, S. R. (1984). A Model for Flow in Meandering Streams. *Water Resources Research*, 20(9), 1301–1315. <https://doi.org/10.1029/WR020i009p01301>
- Thompson, D. M., Wohl, E. E., & Jarrett, R. D. (1999). Velocity reversals and sediment sorting in pools and riffles controlled by channel constrictions. *Geomorphology*, 27(3–4), 229–241. [https://doi.org/10.1016/s0169-555x\(98\)00082-8](https://doi.org/10.1016/s0169-555x(98)00082-8)
- van Rijn Leo C. (2007). Unified View of Sediment Transport by Currents and Waves. I: Initiation of Motion, Bed Roughness, and Bed-Load Transport. *Journal of Hydraulic Engineering*, 133(6), 649–667. [https://doi.org/10.1061/\(ASCE\)0733-9429\(2007\)133:6\(649\)](https://doi.org/10.1061/(ASCE)0733-9429(2007)133:6(649))
- Venditti, J. G., Dietrich, W. E., Nelson, P. A., Wydzga, M. A., Fadde, J., & Sklar, L. (2010). Mobilization of coarse surface layers in gravel-bedded rivers by finer gravel bed load. *Water Resources Research*, 46(7). <https://doi.org/10.1029/2009WR008329>
- Wilcock, P. R. (1996). Estimating Local Bed Shear Stress from Velocity Observations. *Water Resources Research*, 32(11), 3361–3366. <https://doi.org/10.1029/96WR02277>
- Wilcock, P. R., & Crowe, J. C. (2003). Surface-based Transport Model for Mixed-Size Sediment. *Journal of Hydraulic Engineering*, 129(2), 120–128. [https://doi.org/10.1061/\(ASCE\)0733-9429\(2003\)129:2\(120\)](https://doi.org/10.1061/(ASCE)0733-9429(2003)129:2(120))
- Wood, P. J., & Armitage, P. D. (1997). Biological Effects of Fine Sediment in the Lotic Environment. *Environmental Management*, 21(2), 203–217. <https://doi.org/10.1007/s002679900019>
- Yager, E. M., Venditti, J. G., Smith, H. J., & Schmeeckle, M. W. (2018). The trouble with shear stress. *Geomorphology*, 323, 41–50. <https://doi.org/10.1016/j.geomorph.2018.09.008>